Supernova 1987A:30 years later - Cosmic Rays and Nuclei from Supernovae and their aftermaths
Proceedings IAU Symposium No. 331, 2017
A. Marcowith, M. Renaud, G. Dubner, A. Ray & A. Bykov, eds.

doi:10.1017/S1743921317004689

Low frequency radio counterparts of HESS J1731−347 a.k.a SNR G353.6−0.7

A. J. Nayana and Poonam Chandra

National centre for Radio Astrophysics
Tata Institute of Fundamental Research
PO Box 3, Pune 411007
email: nayana@ncra.tifr.res.in
email: poonam@ncra.tifr.res.in

Abstract. HESS J1731−347 a.k.a. SNR G353.6−0.7 is one of the five known very high energy (VHE, Energy > 0.1 TeV) shell-type supernova remnants. We carried out Giant Metrewave Radio Telescope (GMRT) observations of this TeV SNR in 1390, 610 and 325 MHz bands. We detected the 325 and 610 MHz radio counterparts of the SNR G353.6−0.7 (Nayana *et al.* 2017). We also determined the spectral indices of individual filaments and our values are consistent with the non-thermal radio emission. We compared the radio morphology with that of VHE emission. The peak in radio emission corresponds to the faintest feature in the VHE emission. We explain this anti-correlated emission in a possible leptonic origin of the VHE γ-rays.

Keywords. acceleration of particles–radiation mechanisms: non-thermal–cosmic rays–ISM: individual objects:SNR G353.6−0.7–ISM: supernova remnants–radio continuum: ISM.

1. Introduction

The origin of Galactic cosmic rays remains a fundamental question since its discovery. Supernova remnant (SNR) shocks are considered as one of the possible sites of particle acceleration to cosmic ray energies (Blasi 2013). A very high energy (VHE; Energy > 100 GeV) shell like γ-ray source associated with a SNR provides a unique opportunity to study particle acceleration in SNR shocks. However, there are only five SNRs with spatially resolved shell like VHE emission (Acero *et al.* 2015). These are RX J1713.7−3946 (Aharonian *et al.* 2004), RX J0852.0−4622 (Aharonian *et al.* 2007), RCW 86 (Aharonian *et al.* 2009), SN 1006 (Acero *et al.* 2010) and HESS J1731−347 (Abramowski *et al.* 2011). HESS J1731−347 was discovered in the HESS Galactic plane survey as an unidentified VHE γ-ray source (Aharonian *et al.* 2008). A faint shell-like radio source SNR G353.6−0.7 with a diameter of $\approx$ 30' was identified in spatial coincidence with this VHE source by Tian *et al.*(2008) in the 1.4 GHz southern Galactic plane survey (SGPS) map (Haverkorn *et al.* 2006) and the 843 MHz Molonglo Galactic plane survey (MOST) map (Green *et al.* 1999). A deeper γ-ray observation of HESS J1731−347 revealed shell like morphology (Abramowski *et al.* 2011) and it became the fifth member of the VHE shell-SNR group. X-ray emission was detected from HESS J1731−347 in the archival *ROSAT* data (Aharonian *et al.* 2008; Tian *et al.* 2008). The non-thermal X-ray emission attests the presence of electron population of TeV energies in the SNR (Tian *et al.* 2010; Abramowski *et al.* 2011; Bamba *et al.* 2012). A central compact object (CCO) was detected in the geometric centre of the SNR using archival *XMM-Newton* data (Halpern & Gotthelf 2010).

We carried out the 325, 610 and 1390 MHz observations of the SNR G353.6−0.7 with the Giant Metrewave Radio Telescope (GMRT) and detected the SNR at 325 and 610 MHz. we determined the spectral indices of bright individual filaments. We also

compared the radio morphology with that of the VHE emission. Our results are published in (Nayana *et al.* 2017) and here we summarize the results presented in (Nayana *et al.* 2017).

2. GMRT observations and data analysis

We observed SNR G353.6−0.7 in the 325, 610 and 1390 MHz bands with the GMRT. The GMRT primary beams at 325, 610 and 1390 MHz are 85.2, 43 and 26.2 arcmin respectively. Since the SNR is 30' in diameter, a single pointing was done at 325 and 610 MHz whereas four pointings were done at 1390 MHz to cover the full extent of the SNR. Flux density calibrator was observed in the beginning and end of each observing run at all frequencies to calibrate antenna gains. Phase calibrator was observed in regular intervals through out the observing run to calibrate for phase variations due to ionospheric fluctuations. The phase calibrator was used for bandpass calibration as well. The observing bandwidth was 33 MHz split into 256 channels at all frequencies.

The data were analysed using Astronomical Image Processing System (AIPS). Initial flagging and calibration was done using standard AIPS tasks. Calibration was done for single channel and the solutions were applied to all the channels. Bandpass calibration was done using the phase calibrator. Few channels were averaged in the target source data so as to reduce the effect of bandwidth smearing. Initially high resolution images were made using visibility data from baselines greater than 1 km, i.e. excluding the GMRT central square data. Few rounds of phase only self-calibration and 2 rounds of amplitude and phase self-calibration was performed. All the clean components were subtracted from the uv data and low resolution image was made using small uv range i.e only the central square data. This procedure was followed to remove the compact sources in the field and image the extended structure of the SNR with better sensitivity.

The SNR was detected in the 325 and 610 MHz bands. We did not detect the SNR at 1390 MHz due to the sensitivty limitation and the lack of short baselines.

3. Results and discussion

3.1. *Morphology of the SNR*

We detected SNR G353.6−0.7 at 325 and 610 MHz frequencies (Fig. 1) with an angular extent of 30 arcmin (Nayana *et al.* 2017). The shell structure of the SNR with filaments is clearly seen in the 325 MHz GMRT map whereas the SNR is partially detected in the 610 MHz map (Fig. 1, top panels). The brightest filament in the 325 and 610 MHz map is the south-east filament. The faintest emission is from the northern region of the SNR which is not detected in the 610 MHz map due to sensitivity limitation. The brightest filaments seen in 325 and 610 MHz GMRT maps are also seen in 1.4 GHz SGPS map and 843 MHz MOST map (Fig. 1, bottom panels). A compact source is seen inside the SNR in the 1.4 GHz SGPS map and 843 MHz MOST map (Fig. 1, bottom panels) which is not seen in the 325 and 610 MHz GMRT maps (Fig. 1, top panels). This is due to the point source subtraction done before making low resolution images in our analysis. The compact source seen towards the west of the SNR is a H_{II} region (Condon *et al.* 1998). The extended wing like emission seen further west is likely to originate in H_{II} regions since these regions show bright emission in 60 μm IRAS map (Neugebauer *et al.* 1984) and 22 μm WISE map (Wright *et al.* 2010). The integrated flux density of the SNR at 325 MHz is 1.84 ± 0.15 Jy. Assuming a typical spectral index of −0.5 for SNRs (Jones *et al.* 1998), we obtained a flux density of 0.88 Jy at 1420 MHz. Tian *et al.*(2008) reported the

https://doi.org/10.1017/S1743921317004689 Published online by Cambridge University Press

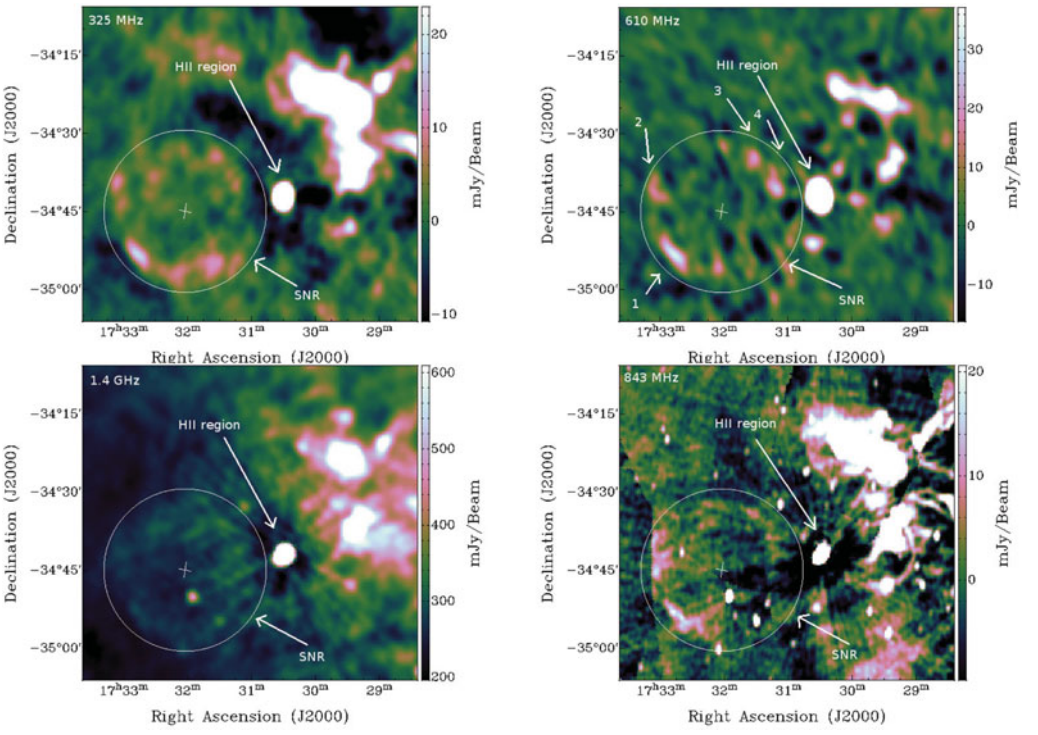

Figure 1. *Top left*: The GMRT low resolution map of the field containing SNR G353.6−0.7 at 325 MHz. Map resolution is 135×97 arcsec^2 and the rms is 4.8 mJy beam^{-1}. *Top right*: The GMRT low resolution map of the field containing SNR G353.6−0.7 at 610 MHz. Map resolution is 150×105 arcsec^2 and the rms is 4 mJy beam^{-1}. Here the areas marked by 1, 2, 3, 4 are the filaments for which the spectral indices were estimated. Compact sources have been removed from both the 325 and 610 MHz GMRT maps. For comparison, we show the SGPS map (Haverkorn *et al.* 2006) of the field containing SNR G353.6−0.7 at 1420 MHz with a resolution of 100×100 arcsec^2 and an rms of 10 mJy beam^{-1} (*bottom left*), as well as the MOST map (Green *et al.* 1999) of the field containing SNR G353.6−0.7 at 843 MHz with a resolution of 49.71×43.00 arcsec^2 and an rms of 3 mJy beam^{-1} (*bottom right*). The circles in all four images are of the same size and centred at the CCO position (marked with a cross) and indicate the area enclosing SNR G353.6−0.7. The colour scheme used in the maps is cubehelix (Green 2011). Figure reproduced from (Nayana *et al.* 2017).

flux density of SNR G353.6−0.7 as 2.2 ± 0.9 Jy at 1420 MHz from combined Australia Telescope Compact Array and Parkes telescope data. Our flux density estimation at 1420 MHz match within 1.5σ with that reported by Tian *et al.* (2008).

3.2. *Spectral Index*

Spectral indices were determined for the four prominent filaments detected in both 325 and 610 MHz maps (Fig. 1, top panel). The spectral index values of filament 1,2,3 and 4 are −0.70 ± 0.19, −1.11 ± 0.22, −0.50 ± 0.30 and −0.15 ± 0.32 respectively. The spectral indices are broadly consistent with the non-thermal synchrotron emission. The flux densities of each filament at 325 and 610 MHz and their physical dimensions in angular units are listed in Table1. The spectral index of filament 2 = −1.11±0.22 seems to be steeper than the typical synchrotron spectral index (α=−0.5). This steepening is consistent with the synchrotron cooling and could be indicative of a higher magnetic field strength in that region of the SNR.

https://doi.org/10.1017/S1743921317004689 Published online by Cambridge University Press

Table 1. Physical dimensions of four filaments and flux densities at 325 and 610 MHz.

Filament	Length (arcmin)	Width (arcmin)	S_{int}(325 MHz) (mJy)	S_{int}(610 MHz) (mJy)	Spectral Index
Filament 1	11	3	106.22	68.67	-0.70 ± 0.19
Filament 2	6	2.8	121.66	58.94	-1.11 ± 0.22
Filament 3	5.4	3.7	56.90	41.55	-0.50 ± 0.30
Filament 4	5.9	3.4	42.99	39.45	-0.15 ± 0.32

Notes:
[1] S_{int}(610 MHz) and S_{int}(325 MHz) denoted the integrated flux density of the filaments at 610 and 325 MHz respectively.

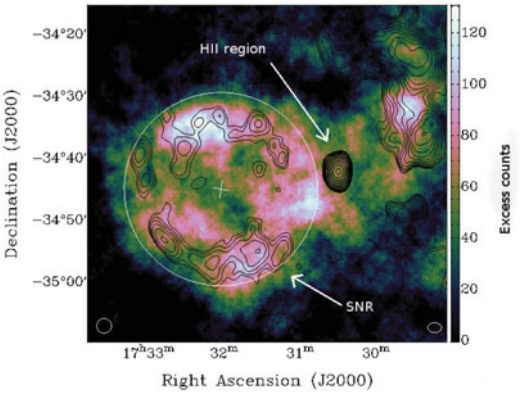

Figure 2. TeV γ-ray excess map (Abramowski *et al.* 2011) (resolution 144×144 arcsec^2; shown in the bottom left corner) overlaid with the GMRT 325 MHz map (resolution 135×97 arcsec^2; shown in the bottom right corner) contours. The scale of the γ-ray excess map is excess counts per smoothing gaussian width (σ = 0.04 deg). The contours are $\pm\sqrt{2}^n\sigma$ mJy beam^{-1} ($n = -2, 2, 3, 4, 5, 6$; σ=1.5 mJy beam^{-1}). The circle indicates the area enclosing SNR G353.6−0.7 centred at the CCO position (marked with a cross). The colour scheme used in the map is cubehelix (Green 2011). Figure reproduced from (Nayana *et al.* 2017).

3.3. *Comparison with the VHE emission*

We compared the low frequency radio morphology revealed in the GMRT maps with the VHE emission in the HESS map (Fig. 2). The shell like morphology of the SNR is clearly seen in both radio and VHE emission. The spatial extent of radio emission fairly overlaps with that of VHE emission except towards the west of the SNR. Here, the VHE emission is bright but the radio emission is not detected above the sensitivity limit of the map. The emission in radio and VHE does not seem to be correlated. The brightest filaments in the radio are the south-east and the eastern filaments (Fig. 2) which are faintest in the VHE emission. The peak in VHE emission (northern filament) corresponds to the faintest filament in radio. The variation in radio brightness can be due to the variation of magnetic field strength or due to the variation of ambient interstellar medium (ISM) density. A density gradient in the ambient ISM can happen if there is an encounter of SNR shock with a nearby molecular cloud. So far no evidences for such an interaction is reported in the case of SNR G353.6−0.7. The ^{12}CO spectrum derived from the vicinity of SNR G353.6−0.7 does not show any kinematic signatures of a possible interaction of the SNR shock with a molecular cloud (Abramowski *et al.* 2011). Thus the azimuthal variation of radio brightness is most likely due to the variation of the magnetic field

https://doi.org/10.1017/S1743921317004689 Published online by Cambridge University Press

strength. The spectral indices of different filaments of the SNR G353.6−0.7 indicate the azimuthal variation of magnetic field (Table 1). Here the spectral index of filament 2 is −1.11 which is roughly 0.5 steeper compared to the typical SNR spectral index of −0.5, consistent with synchrotron cooling, indicating higher magnetic field in this filament. Thus the magnetic field strength is relatively high in the region of the south-east and eastern filaments. Since radio emissivity is proportional to $B^{3/2}$, these filaments are bright in radio. If the VHE γ-rays are produced due to inverse compton scattering of photons, there are fewer IC electrons in this region due to synchrotron cooling and hence the VHE emission is faint here. The magnetic field strength is low towards the northern region of the SNR, and this causes the effect of synchrotron cooling to be weak and the IC emission becomes dominant. Towards the west, magnetic field strength is likely to be similar to or less than that of the northern region, and the synchrotron emission is below the sensitivity limits where VHE emission is bright. Thus we explain the anti-correlated emission seen in SNR G353.6−0.7 in radio and VHE γ-rays in a possible leptonic scenario.

4. Summary

We summarize the results presented in Nayana *et al.* (2017). We observed HESS J1731−347 also known as SNR G353.6−0.7 with the GMRT at 325, 610 and 1390 MHz and detected the radio morphology of the SNR G353.6−0.7 at 325 and 610 MHz. The complete shell morphology of the SNR is seen at 325 MHz and the SNR is partially seen at 610 MHz. The integrated flux density of the SNR G353.6−0.7 at 325 MHz is 1.84 ± 0.15 Jy. We also determined the spectral indices of four bright filaments of the SNR G353.6−0.7. The spectral index values range from −0.15 to −1.11, consistent with the non-thermal emission. We compared the low frequency radio morphology with VHE γ-ray emission. The brightest feature in radio correspond to the faintest feature in the VHE emission. we explain this anti-correlated emission in a leptonic scenario of γ-ray emission.

References

Acero, F., Aharonian, F., Akhperjanian, A. G., *et al.* 2010, *A&A*, 516, A62
Acero, F., Lemoine-Goumard, M., Renaud, M., *et al.* 2015, *A&A*, 580, A74
Aharonian, F. A., Akhperjanian, A. G., Aye, K.-M., *et al.* 2004, *Nature*, 432, 75
Aharonian, F., Akhperjanian, A. G., Bazer-Bachi, A. R., *et al.* 2007, *ApJ*, 661, 236
Aharonian, F., Akhperjanian, A. G., Barres de Almeida, U., *et al.* 2008, *A&A*, 477, 353
Aharonian, F., Akhperjanian, A. G., de Almeida, U. B., *et al.* 2009, *ApJ*, 692, 1500
Bamba, A., Pühlhofer, G., Acero, F., *et al.* 2012, *ApJ*, 756, 149
Blasi, P. 2013, *A&AR*, 21, 70
Condon, J. J., Cotton, W. D., Greisen, E. W., *et al.* 1998, *AJ*, 115, 1693
Green, A. J., Cram, L. E., Large, M. I., & Ye, T. 1999, *ApJS*, 122, 207
Green, D. A. 2011, *Bulletin of the Astronomical Society of India*, 39, 289
Halpern, J. P. & Gotthelf, E. V. 2010, *ApJ*, 710, 941
Haverkorn, M., Gaensler, B. M., McClure-Griffiths, N. M., Dickey, J. M., & Green, A. J. 2006, *ApJS*, 167, 230
H. E. S.. S. Collaboration, Abramowski, A., Acero, F., *et al.* 2011, *A&A*, 531, A81
Jones, T. W., Rudnick, L., Jun, B.-I., *et al.* 1998, *PASP*, 110, 125
Nayana, A. J., Chandra, P., Roy, S., *et al.* 2017, *MNRAS*, 467, 155
Neugebauer, G., Habing, H. J., van Duinen, R., *et al.* 1984, *ApJ* (Letters), 278, L1
Tian, W. W., Leahy, D. A., Haverkorn, M., & Jiang, B. 2008, *ApJ* (Letters), 679, L85
Tian, W. W., Li, Z., Leahy, D. A., *et al.* 2010, *ApJ*, 712, 790
Wright, E. L., Eisenhardt, P. R. M., Mainzer, A. K., *et al.* 2010, *AJ*, 140, 1868